PCCP

PAPER

View Article Online
View Journal | View Issue

Cite this: *Phys. Chem. Chem. Phys.*, 2025, **27**, 11628

Implications of magnetic dilution of $PrFeO_3$ with Bi^{3+} on its dielectric and magnetic properties†

Shivangi Rao, [a] Subhajit Sau, [b] V. Kanchana, [b] G. Vaitheeswaran *[c] and Rajamani Nagarajan *[a]

Research on functional oxide ceramics has tremendous translational potential for technological applications. Despite sharing a similar formula, $BiFeO_3$ and $REFeO_3$ (RE = rare earth) perovskites differ widely in structure and properties. The potential of substituting non-magnetic Bi^{3+} with a stereochemically active $6s^2$ lone pair in rare-earth ferrites remains largely unexplored. In this work, the consequences of replacing Pr^{3+} with Bi^{3+} on the dielectric and magnetic properties of $PrFeO_3$ were investigated by synthesizing the samples using a solution combustion method. The inclusion of bismuth led to local site disorder and promoted the reduction of more amounts of Fe^{3+} to Fe^{2+}, as verified by Raman and XPS measurements. The higher concentration of Fe^{2+} resulted in the formation of oxygen vacancies. The band gaps of the pure and Bi-substituted $PrFeO_3$ samples were in the range of 1.90–2.08 eV. The field and temperature-dependent magnetic measurements of $Pr_{1-x}Bi_xFeO_3$ confirmed the magnetic dilution. ZFC and FC measurements at low fields revealed a spin reorientation transition at 101 K in the case of $Pr_{0.70}Bi_{0.30}FeO_3$, which supported the negative exchange bias effect at room temperature. The dielectric constant increased with an increase in bismuth content. Electronic structure calculations with charge density plots revealed the induction of polarization by the electric field in the Bi^{3+}-containing samples. This was also verified through PUND measurements, which showed the existence of intrinsic and switchable polarization (0.17 μC cm^{-2}). The random distribution of the stereochemically active $6s^2$ lone pair on Bi^{3+} has been proposed as the reason for the observed polarization.

Received 1st January 2025,
Accepted 28th April 2025

DOI: 10.1039/d5cp00004a

rsc.li/pccp

1 Introduction

Solids with a perovskite structural arrangement are the prototype for demonstrating any application among the materials science community.[1–4] The perovskite structure's flexibility to accommodate multiple substitutions with suitable cations, exhibiting diverse symmetries, allows researchers to tailor their functions based on optical, electrical, magnetic, and catalytic properties.[1–4] The halide-based perovskites deserve special mention as they offer better possibilities for a renewable, sustainable energy conversion source.[5] Although the perovskite structure is ideally cubic, structural deviations from distortion can lower its symmetry to tetragonal, orthorhombic, rhombohedral, monoclinic, and triclinic.[2–4] The distortion in the perovskite structure in compounds made under ambient pressure and temperature conditions has been correlated to the Goldschmidt tolerance factor (t) involving the ionic radii of the constituent ions.[6] Structurally distorted perovskite oxides occur when 't' is less than unity, modifying their electrical and magnetic properties. The most common distortion is the tilting/rotation of the rigid BO_6 octahedra imposed by the small size of the A-cation while maintaining their corner-sharing connectivity.[6] Despite sharing a similar formula, $BiFeO_3$ and $REFeO_3$ (RE = rare earth) perovskites differ widely in their structure and properties.[7–11] While $BiFeO_3$ has a rhombohedrally distorted structure, $REFeO_3$ exhibits orthorhombic distortion. $BiFeO_3$ crystallizes in the non-centrosymmetric space group ($R3c$ (#161)), where the cuboctahedral and octahedral positions of the perovskite unit cell are occupied by Bi^{3+} and Fe^{3+} ions, respectively. Displacement of Bi^{3+} ions from their center of symmetry along the [111]c direction and antiphase-rotated FeO_6 units along the rhombohedral axis (Glazer notation $a^-a^-a^-$) are present in the structure.[1–4] Due to the stereoactive lone pair of electrons ($6s^2$), the Bi^{3+} ions have a more significant displacement compared to Fe^{3+} ions, resulting in

[a] *Materials Chemistry Group, Department of Chemistry, University of Delhi, Delhi-110007, India. E-mail: 18darklotus@gmail.com, rnagarajan@chemistry.du.ac.in*
[b] *Department of Physics, Indian Institute of Technology Hyderabad, Kandi, Medak-502285, Telangana, India. E-mail: ph21resch01001@iith.ac.in, kanchana@phy.iith.ac.in*
[c] *School of Physics, University of Hyderabad, Prof. C. R. Rao Road, Gachibowli, Hyderabad 500046, Telangana, India. E-mail: vaithee@uohyd.ac.in*

† Electronic supplementary information (ESI) available: Details of synthesis, characterization, refinement results, magnetic configurations of $PrFeO_3$, results of magnetic and ferroelectric measurements. See DOI: https://doi.org/10.1039/d5cp00004a

ferroelectric ordering ($T_C \sim 830$ °C) and antiferromagnetic (AFM) ordering ($T_N \sim 370$ °C).[7–9] The magnetic moments of Fe^{3+} in $BiFeO_3$ show a G-type antiferromagnetic (AFM) arrangement.[7–9] On the other hand, rare-earth orthoferrites ($REFeO_3$; RE = Pr–Lu) show orthorhombic distortion of the perovskite structure crystallizing in the non-polar *Pnma* (#62) space group. Its symmetry is described by an in-phase tilt of FeO_6 octahedra in the *a*-direction and out-of-phase tilt of FeO_6 octahedra in the *b*- and *c*-directions (Glazer notation $a^+b^-b^-$).[10] While the Bi^{3+} ion in $BiFeO_3$ has an eight-fold coordination with oxygen, the RE^{3+} ion in $REFeO_3$ is a pseudo-twelve-coordinated polyhedron with eight first-nearest oxygen atoms and four second-nearest oxygen atoms. Of the two magnetic sublattices in $REFeO_3$, Fe^{3+}–Fe^{3+} exchange interactions dominate over those of Fe^{3+}–RE^{3+} and RE^{3+}–RE^{3+}, which causes the spins to order near 650–700 K with a slightly canted G-type AFM arrangement.

In the search for materials exhibiting a large electrical polarization along with the magnetic ordering, researchers consider rare-earth orthoferrites as an alternative to $BiFeO_3$, Aurivillius phases, $PbZrO_3$, and $PbTiO_3$.[12–20] $NdFeO_3$, $SmFeO_3$, $GdFeO_3$, $DyFeO_3$, and $HoFeO_3$, despite crystallizing in centrosymmetric space groups (*Pnma*/*Pbnm*) showed ferroelectricity facilitated by the exchange striction caused by the spin-exchange interaction between the 4f- and 3d-ion-containing sublattices.[14–19] In the case of $YFeO_3$ (containing a non-magnetic Y^{3+} ion), the origin of ferroelectricity is attributed to the antisite defects, creating a net local dipole moment.[12] Hence, taking a magnetic orthoferrite and diluting the A-site with a non-magnetic trivalent ion assumes greater significance as it can bring in more clarity on the origin of ferroelectricity in rare-earth orthoferrites.

The Bi^{3+} ion has a stereochemically active $6s^2$ lone pair, and introducing such a metal ion in rare-earth orthoferrites can perform the dual functions of applying chemical pressure and introducing possible polarization under applied electric fields. It is worth noting that theoretical simulations have demonstrated a large enough epitaxial misfit strain (compressive and tensile) to induce improper ferroelectricity in $REFeO_3$ thin films.[21–23] The consequences of including non-magnetic Bi^{3+} in place of magnetic RE^{3+} or non-magnetic Y^{3+} in the $REFeO_3$ system are quite limited.[24–28] The results from these studies are divergent, yielding fewer answers but many questions. In the case of $LaFeO_3$, the bismuth inclusion caused the reduction of Fe^{3+} to Fe^{2+}, leading to oxygen vacancies, whereas, in $Bi_{0.50}Nd_{0.50}FeO_3$, the exclusive presence of Fe^{3+} was deduced.[24–27] While the weak ferromagnetic behavior became stronger with bismuth substitution in $LaFeO_3$, further weakening in the ferromagnetic behavior was noticed in another report.[25,26] Importantly, ferromagnetic and antiferromagnetic coupling leads to an exchange bias effect in bismuth-substituted $LaFeO_3$ samples.[26] Quite a few reports have dealt with the outcome of Bi-substitution in $PrFeO_3$ and none has investigated the physical property changes introduced by Bi^{3+}. The existence of two redox couplets ($Pr^{4+/3+}$ and $Fe^{3+/2+}$) may be a possible reason for the availability of less reports as they may hinder their synthesis and such an investigation can contribute to an understanding of the role of bismuth in modulating its properties.[29] From such a study, one can derive crucial information that can link the observations reported earlier in Bi-substituted $LaFeO_3$ and $NdFeO_3$ systems. To address this gap, we investigated the changes in the structure and optical, magnetic, and dielectric properties of $PrFeO_3$ after substituting it with progressive amounts of Bi^{3+} (up to 50 mol%) by preparing the samples employing the combustion method. The results from these experiments have been discussed in detail. The encouraging results from the density functional theory (DFT) calculations about the possibility of electric field polarization in Bi^{3+}-containing $PrFeO_3$ samples have been verified from experiments.

2 Experimental details

2.1 Synthesis

The synthesis of $Pr_{1-x}Bi_xFeO_3$ (x = 0.00, 0.10, 0.20, 0.30, 0.40, and 0.50) was carried out following an auto-combustion process using Pr_2O_3 (99.9%, Sigma Aldrich), Bi_2O_3 (99.999%, Sigma Aldrich), iron metal powder (98.5%, Central Drug House), citric acid (99%, Central Drug House), and HNO_3 (68% v/v, Merck).[3] The amounts of reactants used in the synthesis are tabulated in Table S1 (ESI†). Double-distilled water was used for the entire synthetic procedure. Stoichiometric quantities of Pr_2O_3 and Bi_2O_3 were dissolved separately in a minimum amount of dilute HNO_3 (1 : 1 (v/v)). The required amounts of iron metal powder were dissolved separately in a minimum quantity of concentrated HNO_3 by heating (~200 °C) to get a clear orange solution. These solutions were mixed thoroughly with the help of a magnetic stirrer, to which fuel (citric acid solution in water), in the fuel-to-oxidizer ratio of 0.30, was added. Intense brown-colored flaky ashes resulted after the ignition process when the solution was evaporated to dryness at 200 °C. The samples with x up to 0.20 were calcined in the air at 800 °C for 12 h, followed by natural cooling to room temperature (RT). For stoichiometries of $x > 0.20$, the samples were calcined in a flowing argon atmosphere at 800 °C for 12 h.

2.2 Characterization details

A high-resolution Rigaku X-ray diffractometer (MiniFlex600), equipped with a xenon proportional detector engaging Cu K_α radiation (λ = 1.5418 Å), was employed for collecting the sample's powder X-ray diffraction (PXRD) pattern over a 2θ range of 10–100° with a step size of 0.01° and a scan rate of 0.16 seconds per step at RT (25 °C). The lattice and structural refinements of the PXRD patterns were carried out using the Le Bail and Rietveld methods with the help of the GSAS + EXPGUI program.[30] The DIAMOND (Version 3.0) program was employed to construct the crystal structures. The sample's scanning electron microscopy (SEM) image and information about the constituent elements were obtained with the help of a JEOL 6610LV SEM 500 microscope equipped with an EDS attachment. With the help of an FEI Tecnai G2 F30 microscope (operating at 300 kV), the sample's high-resolution transmission electron microscopy (HRTEM) images and selected area electron diffraction (SAED) patterns were gathered. The sample's global and

local site symmetries were analyzed with the help of Raman spectroscopy using a Renishaw inVia™ microscope system operating with an Ar^+ laser (λ = 532 nm with a resolution of 1 cm^{-1}). Repeated scans were performed on thin pellets of the prepared ceramics and averaged out to get the final spectrum. A PHI 5000 VersaProbe II, FEI Inc., X-ray photoelectron spectrophotometer was used to perform the XPS analysis of the samples. The spectrophotometer employed an Ar^+ ion and C_{60} sputter gun and was operated at 10^{-9} Torr pressure. The core-level spectra were recorded using Al K_α radiation at a pass energy of 50 eV, an electron take-off angle of 90°, and a resolution of 0.1 eV. The chemically distinct species were resolved using a Gaussian distribution fitting procedure using the XPSPEAK41 software. Both the charge and peak-position corrections were carried out using the C 1s peak at 284.8 eV as a reference. The samples' diffuse reflectance spectra (DRS) were recorded using a PerkinElmer Lambda 35 scanning double-beam spectrometer equipped with a 50 mm integrating sphere. The solid samples' electron spin resonance spectra were recorded at RT using a JEOL Model JES-X320 ESR spectrometer operating at an X-band frequency of 8.75–9.65 GHz. Field- and temperature-dependent measurements were conducted using the magnetic property measurement system (MPMS) Excel model manufactured by Quantum Design USA with an applied field of 0.005, 0.01, 0.02 and 0.1 T. Magnetic-field-dependent measurements (±5 T) were performed at 298 and 2 K. The dielectric and ferroelectric measurements were conducted on sintered pellets (sintering done at 800 °C for 6 h) with a diameter of 10 mm. For sintering, the powders were mixed with polyvinyl alcohol (PVA) and pelletized at 10 MPa pressure for 5 min using a hydraulic pellet press. The samples had relative densities of ~90–95% (measured using the Archimedes principle). For measurements, both sides of the pellets were coated with a conducting silver paste (SPI supplies, USA: SPI#05002-AB). The dielectric properties of the samples (thickness > 1 mm) were measured using a Novocontrol impedance analyzer in a wide range of frequencies (10^{-1}–10^6 Hz) at RT. For ferroelectric measurements, the samples with thickness (~ 0.6 mm) were poled electrically in silicon oil at RT under a DC electric field of 1 kV mm^{-1} for 2 h before measuring the polarization and electric field (*P*–*E*) curves using a computer-based automatic *P*–*E* loop tracer system (Model: 20PE 1 kHz 0.1N, Marine India, India) at RT up to an electric field of 20 kV cm^{-1} and 50 Hz frequency. To carry out the capacitance–voltage (*C*–*V*) and positive-up negative-down (PUND) measurement at RT, we employed an Advance *P*–*E* Loop Ferroelectric Test System (Marine India, Model: 0.03PE 2MHZ 1F).

2.3 Computational details

In this study, calculations were carried out within the framework of density functional theory (DFT)[31,32] using the projector-augmented plane-wave (PAW)[33] method as implemented in the VASP package (version 5.4.4).[34,35] We adopted the generalized gradient approximation (GGA) for the exchange–correlation functional with PBESol flavor.[36] The atomic pseudopotentials used in the calculations incorporate the valence electronic configurations of the elements as follows: Pr ($4f^3 6s^2$, version 07Jan2002), Fe ($3d^6 4s^2$, version 03Mar1998), O ($2s^2 2p^4$, version 05Jan2001), Bi ($5d^{10} 6s^2 6p^3$, version 10Feb1998). The d and f electrons were corrected through the DFT+*U* approximation within the Dudarev formalism.[37] We used Hubbard parameter U_{Pr} = 2.8 eV and U_{Fe} = 4 eV for the pristine crystal structure. For the 50% Bi-doped structure we used U_{Pr} = 4.2 eV to match the experimental band gaps measured in this study. We have chosen U_{Fe} = 4 eV, as used in the first-principles calculations for a similar orthoferrite structure with an [FeO_6] octahedral environment.[38,39] The same value was used in rare-earth doped $BiFeO_3$, which is the most frequent value used in the first-principles calculations.[40] Therefore, in this study, we maintain a fixed *U* value for Fe as well while varying the *U* value for Pr in the theoretical calculations in accordance with its changing molar concentration in the experiment. All calculations were performed with a plane-wave energy cutoff of 700 eV, Monkhorst–Pack[41] *k*-mesh 8 × 6 × 8, and the energy convergence criterion was chosen to be 10^{-06} eV. All DFT calculations were carried out using the experimentally determined crystal structure. Band structures were plotted using the Sumo toolkit.[42] The spontaneous polarization was evaluated using the Berry-phase method[43,44] as implemented in VASP. The polarization calculation was performed utilizing both the PBE+*U* and PBE-Sol+*U* exchange functionals to explore their impact.

3 Results and discussion

The PXRD patterns of the calcined precursors with the compositions of $Pr_{1-x}Bi_xFeO_3$ (x = 0.00–0.50) in air and under a flowing argon atmosphere are presented in Fig. 1(a) and Fig. S1 (ESI†). For the samples with x up to 0.20, diffraction peaks related to orthorhombic $PrFeO_3$ (ICSD No: 98-002-7274) are observed in the PXRD patterns when calcined in the air. No other diffraction peaks are observed, signifying the absence of other crystalline secondary/impurity phases within the detection limit of the diffractometer. When the concentration of Bi(x) in $Pr_{1-x}Bi_xFeO_3$ is 0.30, peaks of tetragonal $Bi_2O_{2.5}$ (ICSD No: 98-001-0470) and h-Pr_2O_3 (ICSD No: 98-006-1179) are seen in addition to the peaks of $PrFeO_3$ (Fig. S1, ESI†). As both Pr and Fe can exist in mixed oxidation states, the atmosphere during the synthesis of these samples may be critical to avoid generating secondary phases. Hence, the ashes have been calcined in flowing argon for the compositions with x = 0.30–0.50 in $Pr_{1-x}Bi_xFeO_3$, and in their PXRD patterns, peaks of the orthorhombic structure are present exclusively (Fig. 1(a)). The line profiles of h-Pr_2O_3 and various polymorphic forms of Bi_2O_3 are compared with the observed PXRD pattern of $Pr_{0.50}Bi_{0.50}FeO_3$ in Fig. S2 (ESI†), from which we can rule out their presence in our samples. This reinforces the purity of our samples within the detection limit of the used diffractometer.

The diffracted peaks shift towards lower 2θ values in the PXRD patterns of the samples with increased bismuth content, suggestive of the unit cell expansion caused by the higher ionic radius of Bi^{3+} (1.17 Å VIII-fold coordination) than Pr^{3+} (1.126 Å VIII-fold coordination) (Fig. 1(b)). The increase in the lattice

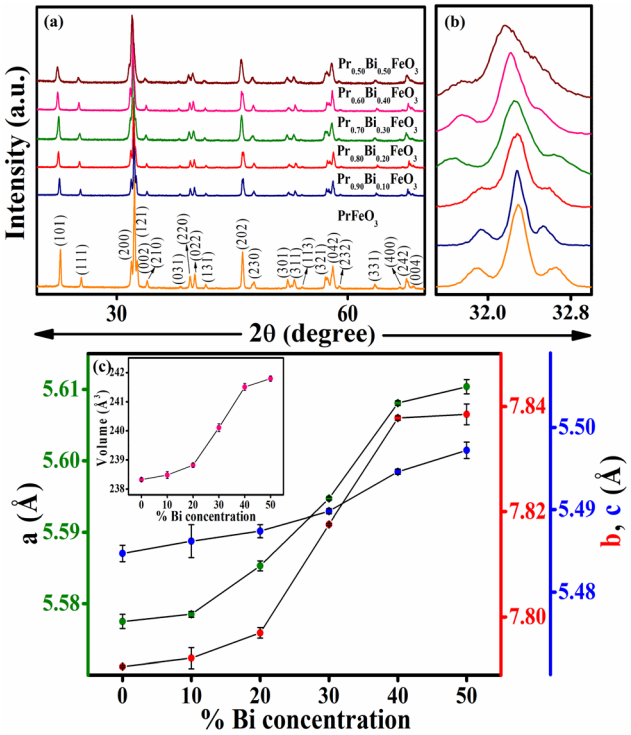

Fig. 1 (a) PXRD patterns of the $Pr_{1-x}Bi_xFeO_3$ series synthesized *via* a combustion route where x = 0.00–0.50, (b) expanded portion of the PXRD patterns of $Pr_{1-x}Bi_xFeO_3$ (31.5–33°), (c) variation of lattice parameters *a*, *b*, and *c* with increasing percentage concentration of Bi. Inset in (c) shows the variation of unit cell volume with increasing bismuth content.

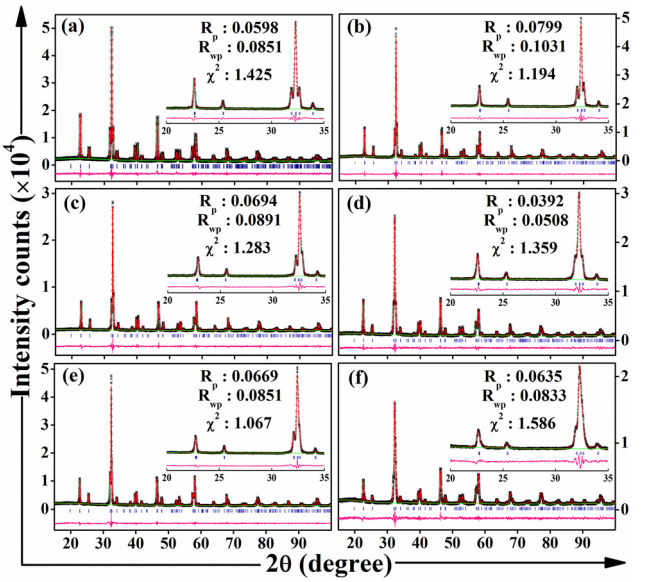

Fig. 2 Structural refinement of the PXRD patterns of $Pr_{1-x}Bi_xFeO_3$ samples by the Rietveld method with x being (a) 0.00, (b) 0.10, (c) 0.20, (d) 0.30, (e) 0.40 and (f) 0.50. Experimental data (black), calculated profile (red), and difference profile (pink) are shown, and the vertical bars (navy) indicate the Bragg positions. The magnified 2θ range of 20–35° is shown in the inset.

parameters becomes more prominent beyond x = 0.20, hinting at the possible contribution from Fe^{2+} having a larger ionic radius.

For the refinement of the PXRD patterns, Pr^{3+} and Bi^{3+} ions were considered to occupy the 4c site, Fe^{3+} ions at the central 4a site at (0,0,0), and O^{2-} ions at the 4c and 8d sites. While the isothermal parameters were refined for both the cations and anions, occupancies were refined for Pr/Bi at the 4c site. The positional parameters of the cations and anions were refined except for the parent composition and Fe^{3+} at the 4a site, as it was a special position in the structure. The experimental and theoretically simulated diffraction patterns converge successfully with satisfactory agreement parameters (Fig. 2). The absence of any unaccounted diffraction peak is verified from the expanded 2θ range shown in the insets of Fig. 2. The atomic parameters from the final cycle of refinements are collected in Table S2 (ESI†). The refinement data show that the concentration of the A-site with Bi in $PrFeO_3$ increases the unit cell constants, with a concomitant increment in the unit cell volume. The increase in the *a* and *b* lattice parameters is quite substantial, while the increase in the *c* parameter is minimal (Fig. 1(c)). The diffracted peaks broaden with increasing bismuth content, indicating local structural changes. The refinement data shows that the Fe–O bond lengths expand as the A-site is concentrated with Bi (Table S3, ESI†). The two Fe–O–Fe angles are not equal to 180° due to the FeO_6 octahedral tilt in the pseudocubic [111] direction. The bond angles gradually increase, preserving the tilted FeO_6 octahedra, implying that the distortion extent decreases with increased Bi content. Still, the distortion is maintained due to the repulsions generated by stereochemically active lone pair of electrons in bismuth. The octahedral tilt angle (ϕ subtracted from the ideal 180°) decreases as the bismuth content increases, maintaining the distortion as shown pictorially in Fig. S3 (ESI†).[28,45]

A porous microstructure morphology with dense crystallites is observed in the SEM images of the samples of $Pr_{1-x}Bi_xFeO_3$ series (x = 0.00–0.50) (Fig. 3(a) and (b) and Fig. S4, ESI†). The average crystallite size distribution of each sample, obtained using the Image J software analyzer, increases from 204–422 nm with the increase in bismuth content in $PrFeO_3$. The EDS spectra of these samples confirm the qualitative presence of Pr, Bi, Fe, and O (Fig. S5, ESI†).

The $PrFeO_3$ and $Pr_{0.70}Bi_{0.30}FeO_3$ samples have also been analyzed using HRTEM and SAED techniques. The HRTEM images support the excellent crystallinity of the as-prepared samples. Both the $PrFeO_3$ and $Pr_{0.70}Bi_{0.30}FeO_3$ samples exhibit a well-resolved lattice fringe in the HRTEM images with the interplanar spacings of 3.49 nm and 2.28 nm corresponding to the (111) and (220) *hkl* planes of the orthorhombic structure (Fig. 3(c) and (e)). The SAED patterns of $PrFeO_3$ and $Pr_{0.70}Bi_{0.30}FeO_3$ show intense spots in a regular array, indicating that the particles are distinctly single crystalline (Fig. 3(d) and (f)). In the SAED patterns of the $PrFeO_3$ and $Pr_{0.70}Bi_{0.30}FeO_3$ samples, the distances between spots correspond to the (331), (301), (004), and (232) *hkl* planes.

The structural and microstructural changes arising from the Bi-substitution in $PrFeO_3$ have been analyzed with the help of

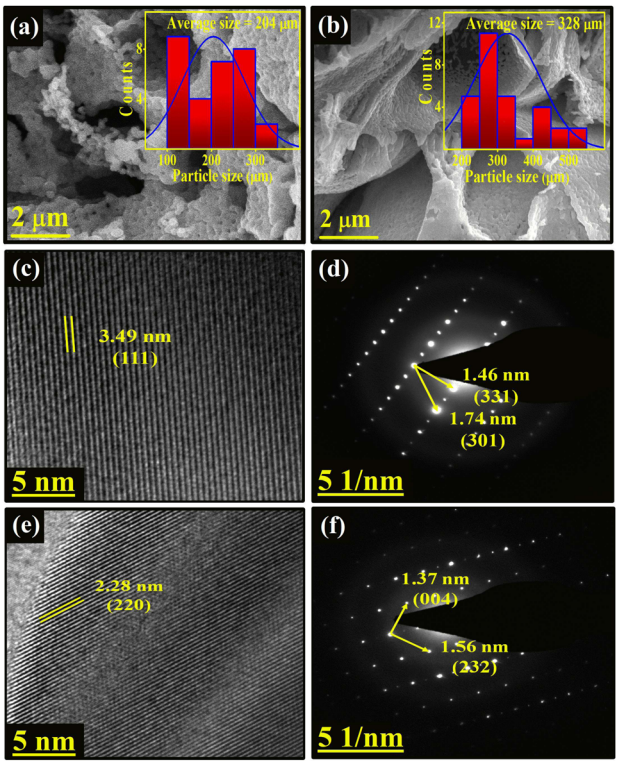

Fig. 3 (a) and (b) SEM images, (c) and (e) HRTEM images, and (d) and (f) indexed SAED patterns of $PrFeO_3$ and $Pr_{0.70}Bi_{0.30}FeO_3$ samples. The histograms in the insets depict the average size distribution.

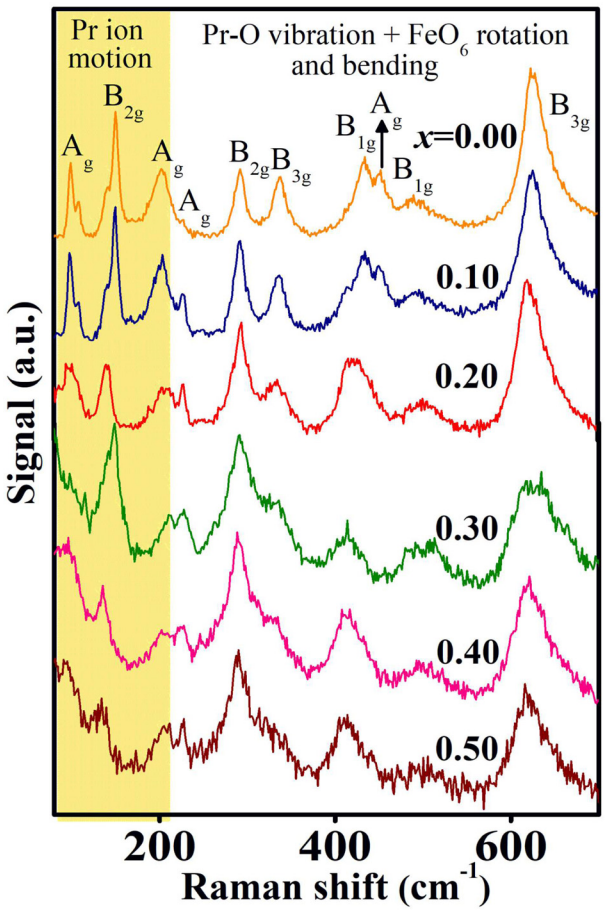

Fig. 4 Raman spectra of $Pr_{1-x}Bi_xFeO_3$ samples (with x = 0.00–0.50) at RT.

Raman spectroscopy. Fig. 4 shows the comparison of the Raman spectra of these samples at RT. Orthorhombic $PrFeO_3$ (*Pnma*) can give rise to 24 Raman-active modes ($7A_g + 5B_{1g} + 7B_{2g} + 5B_{3g}$) and 25 IR modes ($9B_{1u} + 7B_{2u} + 9B_{3u}$).[46] The phonon modes below 200 cm^{-1} are majorly sensitive to displacements of the rare-earth ions (Pr in this case) concerning the FeO_6 octahedra, as highlighted in Fig. 4. The modes between 200 and 300 cm^{-1} relate to the vibrations involving both rare-earth and oxygen ions. The Raman modes above 300 cm^{-1} predominantly correspond to light oxygen ions (involving Fe–O bond lengths and Fe–O_6 rotation and bending). As the four equivalent iron ions occupy the center of inversion in the *Pnma* lattice, one phonon vibration involving them is Raman-inactive.[46,47] The Raman modes below 200 cm^{-1} ($2A_g$ and B_{2g}) and above 400 cm^{-1} ($2B_{1g}$ and B_{3g}) are greatly affected due to Bi's inclusion at the Pr site, among other modes. A considerable shift in the peak positions towards lower wavenumbers, noted for the phonon modes below 200 cm^{-1} and above 400 cm^{-1} ($2B_{1g}$ and B_{3g}), can be due to the substitution of bigger and heavier Bi^{3+} in place of lighter and smaller Pr^{3+}. B_{2g} and B_{3g} modes (at ~300 cm^{-1}) and B_{1g} and A_g modes (at ~450 cm^{-1}) merge for higher Bi concentrations (majorly commencing from x = 0.30). The transition from the sharp features to broad modes with increased bismuth content indicates the introduction of local site disorder. The local distortions include the changes in the preferred coordination number of Bi (pseudo-eight) over Pr (eight) and the deformation of FeO_6 octahedra.[48,49] Such local-site-induced disorder has also been reported in $Bi_{1-x}Pr_xFeO_3$.[50] In the Raman spectra of all the Bi-substituted $PrFeO_3$ samples, no additional band arising from any secondary/impurity phase is seen, confirming their microscopic purity.

As a change in synthesis atmosphere was required for making bismuth-containing samples beyond x = 0.20 in $Pr_{1-x}Bi_xFeO_3$, we were curious to determine the valence states of the constituents of the $PrFeO_3$ and $Pr_{0.70}Bi_{0.30}FeO_3$ samples. Fig. 5(a) shows the XPS survey spectra of the pristine $PrFeO_3$ and $Pr_{0.70}Bi_{0.30}FeO_3$ samples, from which the presence of Pr, Fe, Bi, and O is deduced. The Pr-3d spectrum shows a common line shape characteristic of Pr^{3+}, which, on deconvolution, consists of four peaks at 935.5, 939.5, 956.7, and 960.3 eV (Fig. 5(b)). The peaks with binding energies of 939.5 and 960.3 eV are related to Pr^{3+} ($3d_{5/2}$) and Pr^{3+} ($3d_{3/2}$), and the peaks at 935.5 and 956.7 eV correspond to shakedown satellite peaks arising from well-screened $4f^3$ final states, respectively.[51] The spin–orbit splitting of $3d_{5/2}$ and $3d_{3/2}$ orbitals of praseodymium was found to be ~20.8 eV, consistent with the literature.[52] The mixed oxidation states of Fe in $PrFeO_3$ were revealed from the Fe-2p spectral analysis. The peaks with binding energies of 715.5 ($2p_{3/2}$) and 728.6 ($2p_{1/2}$) eV are due to Fe^{2+} ions, whereas peaks with binding energies of 717.7 ($2p_{3/2}$), 724.5 (satellite peak), and

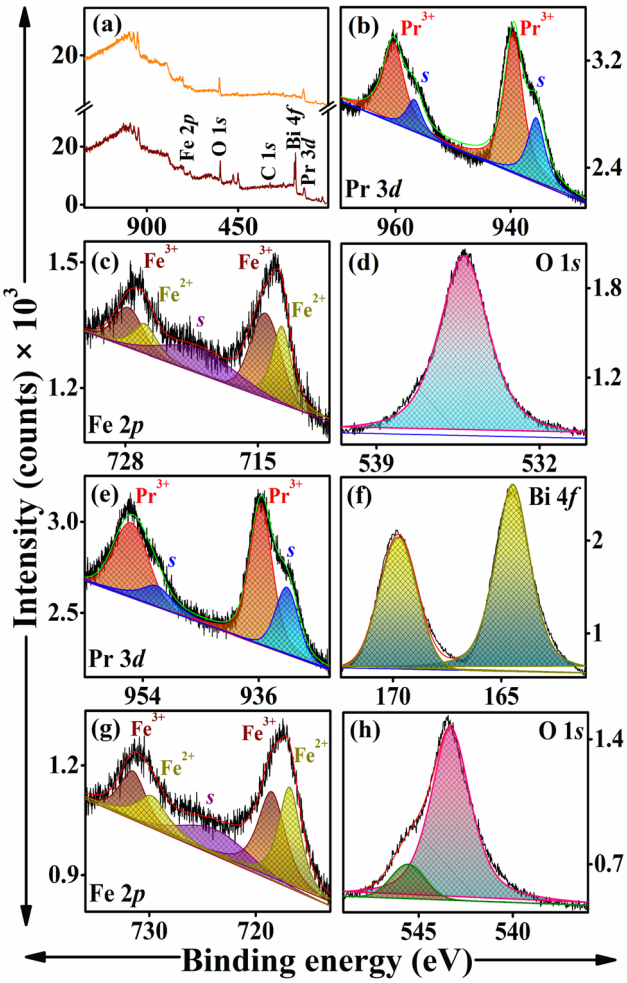

Fig. 5 (a) Survey spectra, (b)–(d) and (e)–(h) core-level spectra of Bi 4f, Pr 3d, Fe 2p, and O 1s of the $PrFeO_3$ and $Pr_{0.70}Bi_{0.30}FeO_3$ samples, respectively. The letter 's' denotes satellite peaks.

731.3 ($2p_{1/2}$) eV correspond to Fe^{3+} ions (Fig. 5(c)). The ratio of the peak area of Fe $2p_{3/2}$ compared to that of $2p_{1/2}$ is 2 : 1, consistent by considering the spin–orbit coupling.[53] From the area under the curve analysis, 43 and 57% of iron exist as Fe^{2+} and Fe^{3+}, respectively. The lattice oxygen appeared at a binding energy of 535.3 eV in the O-1s spectrum (Fig. 5(d)). The Pr-3d spectrum of the $Pr_{0.70}Bi_{0.30}FeO_3$ sample contains peaks with binding energy values of 935.6 and 955.8 eV due to Pr^{3+} ($3d_{5/2}$) and Pr^{3+} ($3d_{3/2}$), and at 931.6 and 951.8 eV due to shakedown satellite peaks, respectively (Fig. 5(e)). The exclusive presence of Bi^{3+} was inferred from the Bi-4f spectrum, showing two peaks at 164.3 ($4f_{7/2}$) and 169.8 eV ($4f_{5/2}$) (Fig. 5(f)). Fe also existed in mixed oxidation states in the Bi-substituted sample, as inferred from the Fe-2p spectrum (Fig. 5(g)). The peaks around 712.7 ($2p_{3/2}$) and 726.1 ($2p_{1/2}$) eV arise from Fe^{2+} ions, and the peaks at the binding energy values of 714.2 ($2p_{3/2}$), 720.6 (satellite peak), and 727.7 ($2p_{1/2}$) eV are related to Fe^{3+} ions. Here again, the areas for $2p_{3/2}$ and $2p_{1/2}$ of Fe-2p confirm the expected ratio of 2 : 1. The $Pr_{0.70}Bi_{0.30}FeO_3$ sample contains 48 and 52% of Fe^{2+} and Fe^{3+}, respectively. A nearly 5% rise in Fe^{2+}-concentration was observed in the $Pr_{0.70}Bi_{0.30}FeO_3$ sample, compared to pristine $PrFeO_3$, promoted by the reducing atmosphere employed for the synthesis. Our observation matches the earlier report in which Fe^{2+} creation due to Bi's inclusion in $LaFeO_3$ is noted.[26] Two peaks at binding energies of 543.4 and 545.3 eV in the O-1s spectrum are attributed to the lattice oxygen (low binding energy) and the oxygen vacancies in the sample. Notably, the peak with the binding energy of 545.3 eV has been attributed to surface-adsorbed hydroxide groups or carbonates (Fig. 5(h)).[54] However, we assign this peak due to oxygen vacancies as we do not observe such a feature in the O-1s spectrum of pure $PrFeO_3$, and an increase in the concentration of Fe^{2+} emerges after substituting with bismuth (30 mol%).[55] The oxygen vacancies are not observed in the pristine sample due to passivation during annealing in air. Further proof of oxygen vacancies in the Bi-substituted sample was gathered from EPR experiments at RT. For comparison, the EPR spectrum of $PrFeO_3$ has also been recorded. A weak EPR signal at a g value of $\sim$2.24 is noticed in the case of $PrFeO_3$, signifying octahedrally coordinated Fe^{3+} ions (Fig. S6, ESI†).[56] The g value keeps decreasing with increasing Bi content and decreases to 2.17 in the case of $Pr_{0.50}Bi_{0.50}FeO_3$, with a subsequent increase in the intensity of the EPR signal. This decrease in the g-value and increase in the EPR signal intensity indicates a gradual increase of localized oxygen vacancies and enhanced Fe–O hybridization (Fig. S6, ESI†).[56,57] Although the increment in linewidth is not uniform, for compositions from x = 0.30–0.50 in $Pr_{1-x}Bi_xFeO_3$, the ΔH is comparatively more compared to the air-annealed samples, corroborating well with the increment in oxygen vacancies, caused possibly by the argon annealing.[58]

The optical absorbance spectra of the $Pr_{1-x}Bi_xFeO_3$ series (x = 0.00–0.50) were recorded to understand the electronic structural changes brought about by bismuth substitution. The maximum absorption edge for $PrFeO_3$ lies at 628 nm (Fig. S7, ESI†). With the introduction of Bi, a gradual red-shift can be seen in the DRS data. A reddish tinge dominates the color of the sample with increasing Bi inclusion. The O–Bi charge transfer transitions appear in the UV region at around 240 and 390 nm. The band in the visible region (at around 485 nm) may be attributed to the charge transfer from the O^{2-} ion to the Fe ion.[28] The bands arising from d–d transitions of octahedrally coordinated Fe^{3+} ions appear as broad transitions in the 705–680 nm range. The broad and diffused transition at around 975–995 nm signifies the $^5T_{2g} \rightarrow {}^5E_g$ transition of Fe^{2+}.[59] Both the direct and indirect band gap values estimated using the Kubelka–Munk function analysis decrease marginally with the inclusion of bismuth in $PrFeO_3$ (Fig. 6). The estimated band gap value of $PrFeO_3$ (E_{direct} = 2.08 eV; $E_{indirect}$ = 1.99 eV) matches well with the values observed earlier.[60] A similar trend is reported earlier in Bi-substituted $GdFeO_3$.[28,29]

We further performed DFT calculations to ascertain the electronic structural changes. To commence with, an examination of the ferromagnetic (FM) and nine additional antiferromagnetic (AFM) spin configurations was done to identify the ground state energy to model the magnetic structure for the pristine composition computationally (Fig. S8, ESI†).

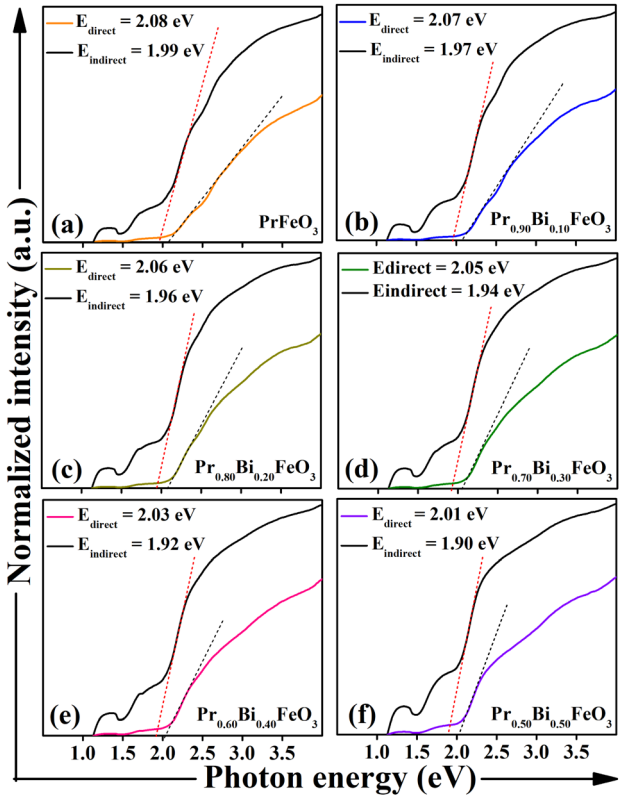

Fig. 6 (a)–(f) Normalized (Kubelka–Munk × energy)^n (n = 2 and 1/2) plots of $Pr_{1-x}Bi_xFeO_3$ (x = 0.00–0.50) samples used for determining the direct and indirect band gaps.

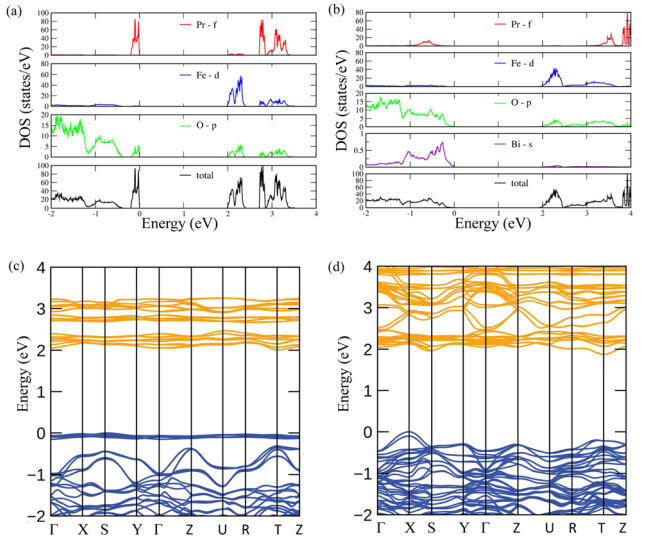

Fig. 7 Partial and total density of states for (a) pristine and (b) 50% Bi-doped $PrFeO_3$. Electronic band structures of (c) pristine and (d) 50% Bi-doped $PrFeO_3$. Band structures plotted along Γ(0,0,0)–X(0.5,0,0)–S(0.5,0.5,0)–Y(0,0.5,0)–Γ–Z(0,0,0.5)–U(0.5,0,0.5)–R(0.5,0.5,0.5)–T(0.0,0.5,0.5)–Z.

These nine AFM configurations included A-, C-, and G-AFM arrangements of Fe. They also account for the spin orientations of Pr atoms positioned within planes at y = 0.25 and y = 0.75, each plane containing 2 Pr atoms. The ground state spin configuration was derived with the Fe atoms arranged in a G-type pattern, whereas the Pr atoms were arranged antiferromagnetically within both of the planes (y = 0.25 and 0.75) but ferromagnetically between the planes y = 0.25 and 0.75 (Fig. S8(h), ESI†). The same configuration gives the ground state structure for $GdFeO_3$ as well.[61] Fig. S9 (ESI†) shows the simulated crystal structures of 50% Bi-substituted $PrFeO_3$, generated by adopting a special quasi-random structure (SQS) approach. Since there are 4 Pr atoms in the unit cell, the desired substitution level can be achieved by replacing 2 of them. This substitution results in three possible combinations of atoms. Furthermore, an additional nine possibilities arise considering the spin arrangements for both Pr and Fe atoms. Among these spin configurations, the lowest energy is achieved when Fe is arranged in a G-AFM configuration with both Pr atoms having an up spin (Fig. S9(b), ESI†). With the aforementioned ground state structure, we calculated electronic structure properties for both pristine and Bi-substituted structures while incorporating spin–orbit coupling (SOC), as shown in Fig. 7.

SOC inclusion becomes important when a heavy element such as Bi is present in the system. For the pristine $PrFeO_3$, the valence band maximum (VBM) consists of major contribution from the Pr-f orbitals, and the conduction band minimum (CBM) is occupied by the Fe-d orbitals with moderate contributions from the O-p orbitals in both the VBM and CBM. On the other hand, a Bi-s contribution arises along with the contributions from the Pr-f and O-p orbitals in the doped scenario in the VBM. The band-structure plots reveal the indirect band gaps of pristine and 50% Bi-substituted $PrFeO_3$ are 1.99 eV (between the S–T point) and 1.92 eV (between the X–T point), respectively. A similar decrement in the direct and indirect band gaps is observed experimentally.

The bismuth inclusion has created mixed valence states of Fe (2+ and 3+) and oxygen vacancies, which can significantly modify the superexchange and magnetic interactions, thereby altering the magnetic properties of $PrFeO_3$. Hence, we measured the magnetic properties of pristine $PrFeO_3$ and Bi-substituted samples. The magnetization of $Pr_{1-x}Bi_xFeO_3$ samples (x = 0.00–0.50) under magnetic fields of ±5 T at 298 and 2 K are shown in Fig. 8(a)–(c) and Fig. S10 (ESI†). At RT, $PrFeO_3$ exhibits a hysteresis loop with considerable ferromagnetic character, characterized by M_r = 0.12 emu g^{-1} and H_c = 0.2 T, aligning well with the earlier report.[62] The anisotropy of the Fe sublattice can contribute to the observed H_c at RT. For the $Pr_{0.70}Bi_{0.30}FeO_3$ sample, the magnetization did not pass through the origin and is horizontally shifted (Fig. 8(b)). This indicates a negative exchange bias resulting from the coupling of ferromagnetic and antiferromagnetic interactions in this sample. We observe only weak ferromagnetism at low temperatures (2 K) for $PrFeO_3$ and Bi-substituted samples (x = 0.10–0.50). The unsaturation, accompanied by reduced magnetization, in all these samples at 2 K suggests the presence of competing weak ferromagnetic and antiferromagnetic interactions.[63] This decrease in magnetization values with Bi^{3+} substitution in $PrFeO_3$ at both RT and 2 K can be attributed to the random

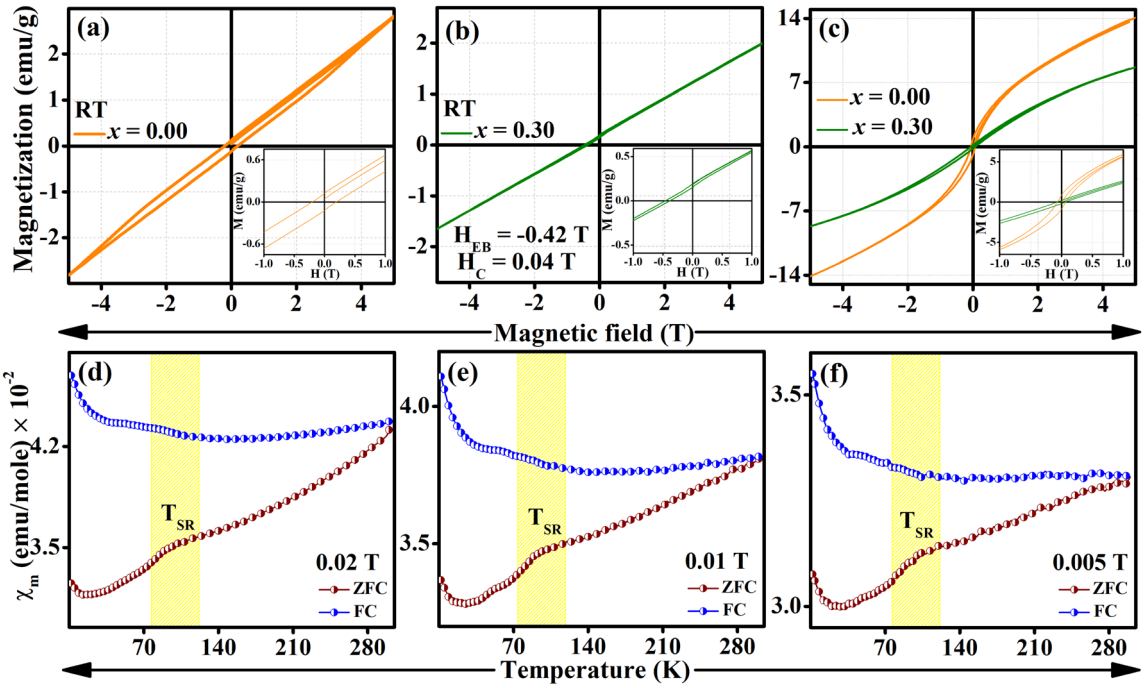

Fig. 8 (a) and (b) Plots of magnetization *vs.* magnetic field for $Pr_{1-x}Bi_xFeO_3$ (x = 0.00 and 0.30) at 298 K and (c) 2 K. (d)–(f) ZFC and FC χ_m *vs.* T plots of $Pr_{0.70}Bi_{0.30}FeO_3$ measured at 0.02, 0.01, and 0.005 T. Expanded portions of the M *vs.* H plots of the $PrFeO_3$ and $Pr_{0.70}Bi_{0.30}FeO_3$ samples are provided as insets in (a)–(c).

distribution of Fe^{3+}, Fe^{2+}, and oxygen vacancies, which causes a slight disruption in the antiferromagnetic superexchange interactions, thereby reducing the overall magnetization. The M_r and H_c values again change with increased Bi content in $Pr_{1-x}Bi_xFeO_3$ at 2 K (Table S4, ESI†). The net magnetization in $PrFeO_3$ and the samples substituted with 10, 20, and 30 mol% Bi at 2 K may originate from spin canting due to tilted FeO_6 octahedra with varying Fe–O–Fe bond angles, altering the Dzyaloshinsky–Moriya interaction.[28] The variation with temperature of the molar susceptibilities of the $Pr_{1-x}Bi_xFeO_3$ samples (x = 0.00–0.50) measured in zero-field-cooled (ZFC) and field-cooled (FC) modes is shown in Fig. 8(d)–(f) and Fig. S11 (ESI†). When these measurements are conducted with a field of 0.1 T, the molar susceptibilities decrease as the temperature increases. Also, the ZFC and FC plots overlap, indicating a typical paramagnetic behavior. The reciprocal of susceptibility ($1/\chi_m$) under FC conditions at H = 0.1 T for pristine and Bi-substituted $PrFeO_3$ in the 2–300 K temperature range is plotted in Fig. S12 (ESI†). All the samples exhibit Curie–Weiss behavior in the 150–300 K range, and below 150 K, antiferromagnetic interactions become dominant. As a significant negative exchange bias is observed in the $Pr_{0.70}Bi_{0.30}FeO_3$ sample, ZFC and FC measurements at lower fields of 0.02, 0.01, and 0.005 T have been conducted, which can provide insight into the spin reorientation transition (SRT) arising from the anisotropy between the RE^{3+} and Fe^{3+} sublattices.[45,62] The ZFC and FC data appear bifurcated during these measurements till room temperature (RT). The creation of Fe^{2+} due to bismuth inclusion and associated oxygen vacancies can bring down the Néel temperature below 700 K.[22] A small hump in the ZFC plot at ~101 K is observed consistently, which can be attributed to the spin reorientation transition temperature (T_{SR}), and it is lower than the T_{SR} reported for $PrFeO_3$ (~140 K).[22]

The effect of bismuth inclusion in place of Pr on the electrical properties of $PrFeO_3$ was investigated by first recording the frequency-dependent (0.1 Hz–0.5 MHz range) dielectric responses at RT. Fig. 9(a) shows the dielectric constants of the $Pr_{1-x}Bi_xFeO_3$ (x = 0.10–0.50) samples as function of frequency. The dielectric constant for all the samples attains a high value (at a low-frequency regime) but decreases as the frequency increases and shows frequency-independent behavior (10^4 Hz onwards). This type of behavior is a general observation of typical dielectrics and is consistent with the combined response of orientational relaxation of dipoles and conduction of charge carriers. At low frequencies, the dipoles get enough time to follow the alternating field, resulting in a higher value of ε', whereas, at a higher frequency, dipoles cannot follow the field, resulting in a decrease in the value of ε'. Usually, the dipolar and interfacial polarizations contribute to the dielectric constant at low frequencies, whereas the electronic and ionic polarizations are dominant contributors at higher frequencies. It is worth noting that the dielectric constant value increases as the Bi content increases in the sample. This observation matches the trend observed in the Bi-substituted $LaFeO_3$ system.[64] $Pr_{0.50}Bi_{0.50}FeO_3$ exhibits the highest value of ε' (1159) among the Bi-containing samples, which indicates the weakening of the Pr–Fe sublattice interaction, matching well with the trend noticed for $Sm_{0.50}Bi_{0.50}FeO_3$.[65]

To understand whether the dielectric response of the samples is due to non-linear dielectric/intrinsic nature or by some

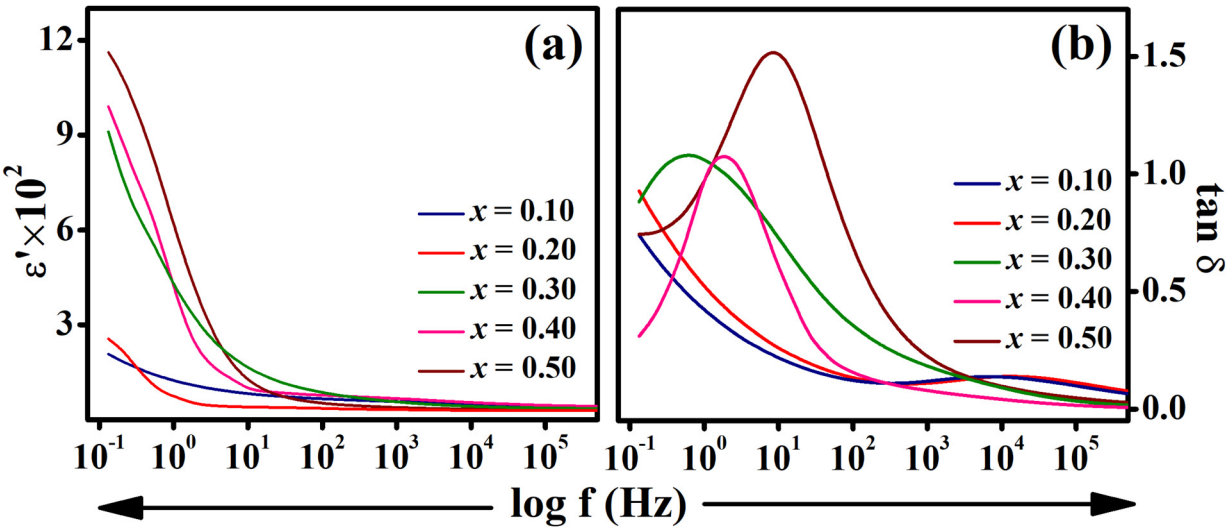

Fig. 9 Frequency dependence of (a) the real dielectric component (ε') and (b) the dielectric loss tangent ($\tan\delta$) of the $Pr_{1-x}Bi_xFeO_3$ samples (x = 0.10–0.50) at RT.

artefact/extrinsic effect, the collected data are analyzed as per the universal dielectric response (UDR) model.[66] According to the UDR model, the relation between conductivity $\sigma'(f)$ and dielectric constant ε' can be expressed as:

$$\sigma'(f) = \sigma_{dc} + \sigma_0 f^s, \quad (1)$$

$$\varepsilon' = (\tan\delta(s\pi/2)\sigma_0(T)f^{s-1})/\varepsilon_0 = A(T)f^{s-1}, \quad (2)$$

where f is the experimental frequency, σ_0 and the exponential factor s ($0 \leq s \leq 1$) are temperature-dependent constants, and ε_0 is the dielectric permittivity of free space. Further, eqn (2) can be described as:

$$f\varepsilon' = A(T)f^s, \quad (3)$$

where

$$A(T) = (\tan\delta(s\pi/2)\sigma_0(T)f^{s-1})/\varepsilon_0.$$

If the frequency-dependent ε' follows the UDR model, it will give a linear behaviour. Fig. S13 (ESI†) shows the best-fit results of $\log(f\varepsilon')$ *vs.* $\log f$ plots. It can be seen that the UDR model is followed in the entire frequency range only by $Pr_{0.90}Bi_{0.10}FeO_3$. For x = 0.20–0.50, the UDR model fits from 10 Hz to 0.5 MHz and deviates at low frequencies. In all cases, the slope lies within the range of 0.06–0.2, indicating close correlation with the UDR model.[66] It appears that at very low frequencies, the localized charge carriers accumulate and give rise to Maxwell–Wagner-type interfacial polarization. In conclusion, the substantially high dielectric constant observed in $Pr_{1-x}Bi_xFeO_3$ systems upon incremental bismuth substitution may arise primarily from electron hopping between Fe^{2+} and Fe^{3+} leading to dipolar polarization and the oxygen vacancies (acting as charge carriers) existing in the grain boundary regions contributing to the space charge polarizations near/across the boundary regions.[67–69] Fig. 9(b) shows the variation of $\tan\delta$ as a function of frequency at RT for $Pr_{1-x}Bi_xFeO_3$ (x = 0.00–0.50). The continuous decrease of dielectric loss with an increase in frequency is a general trend noted in the case of rare-earth ferrites.[70] The samples with $x > 0.20$ show a peak-like behavior between 1 and 100 Hz, reflecting the occurrence of relaxation processes.[65,70] In the low-frequency region, the increased values of $\tan\delta$ can be due to the conductivity and accumulation of electric charge on the inter-crystalline boundaries and structural defects within the Maxwell–Wagner conduction mechanism framework.[71]

The local site distortion caused by Bi^{3+} substitution, together with its stereochemically active lone pair of electrons ($6s^2$), can essentially cause a certain degree of polarization under an applied electric field. The computed spontaneous polarization in the pristine $PrFeO_3$ is almost zero. Further, spontaneous polarization calculations have been carried out utilizing the Berry phase approach for 50% Bi-substituted $PrFeO_3$. The computed value of spontaneous polarization (P_s) comes out to be 0.10 μC cm^{-2}. As a comparative study,[72] polarization was calculated at the PBE and PBEsol levels; both yielded the same results. In the Bi-substituted scenario, the electron localization function was also calculated, and a minor charge density shared between the O^{2-} and Bi^{3+} ions was observed, generating this polar behavior (Fig. 10).

Encouraged by the theoretical calculation results, *P–E* loops of $Pr_{1-x}Bi_xFeO_3$ (x = 0.10–0.40) have been measured at RT and are reproduced in Fig. S14 (ESI†). It is known that the present system is a case of non-classical ferroelectrics and expected to exhibit a leaky ferroelectric behavior as these are measured in ceramic pellets.

In the *P–E* loops of 10 and 20 mol% Bi-substituted $PrFeO_3$ samples, vesica piscis-shaped behavior has been observed. No sharp saturation is noticed in the *P–E* loops of the samples with $x > 0.20$ (recorded at a field of 20 kV cm^{-1}). This leaky behavior may be due to the interfacial polarization receiving contributions from the grain boundary effect, oxygen vacancies, and the multi-valence of iron. Under these circumstances, the true intrinsic polarization may be masked. To deduce actual ferroelectric behavior in these samples, the *C–V* loop of the $Pr_{0.60}Bi_{0.40}FeO_3$ sample is measured in the range of −20 V to +20 V at 50 Hz, and the results are presented in Fig. S15(a) (ESI†). The subtle signature of a

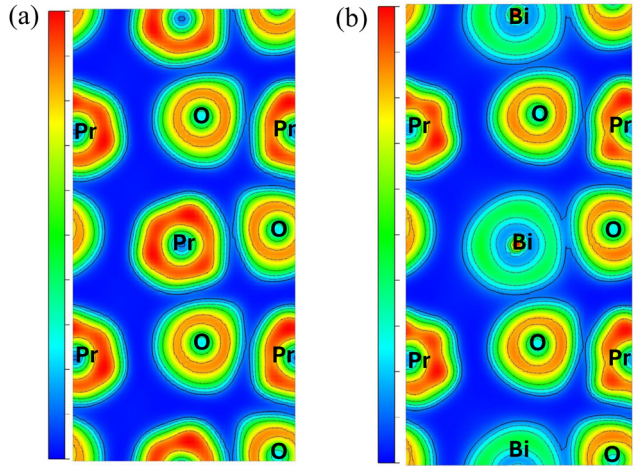

Fig. 10 Electron localization function (ELF) plot for (a) pristine $PrFeO_3$ and (b) 50% Bi-doped $PrFeO_3$.

butterfly-like *C–V* loop with a pair of peaks (typical for a ceramic possessing ferroelectric characteristics) demonstrates polarization reversal in the sample.[15] The butterfly-type shape is the natural result of switching behavior where the maximum occurs near the coercive voltage. To gain further insight into the occurrence of the intrinsic ferroelectric polarization in the sample, the PUND method is employed. The PUND data is collected at RT with a pulse width of 1 ms (Fig. S15(b), ESI†). The measured polarizations during the pulse and in the delay times are designated as P^*, P_r^* and $P^\wedge$, $P_r^\wedge$ in the primary and secondary pulses, respectively, for both the positive and negative top-up sequences. The total polarization (P^*) of 0.778 μC cm^{-2} includes both switched charge density (Q_{SW}) and leakage current, and the second polarization ($P^\wedge$) of 0.603 μC cm^{-2} originates mainly from the leakage current. The difference between the remnant polarization from the switching pulse (P^*) and the non-switching pulse ($P^\wedge$) is equivalent to the net switchable polarization (Q_{SW}). The true switchable polarization ($Q_{SW} = P^* - P^\wedge$) of ~0.175 μC cm^{-2} falls in the same range reported earlier in orthoferrite systems.[73,74] A saturated *P–E* loop is obtained for the $Pr_{0.60}Bi_{0.40}FeO_3$ ceramic sample at RT on applying a 20 kV cm^{-1} field with the maximum P_r (~0.17 μC cm^{-2}) matching closely to the theoretical value of 0.1 μC cm^{-2} (Fig. S15(c), ESI†). Hence, the above results reveal that the sample contains some ferroelectric component introduced locally, within the global centrosymmetric structure, by the random distribution of the stereochemically active $6s^2$ lone pair on Bi^{3+}.[13,73,74] Our results demonstrate that including Bi^{3+} with a stereochemically active lone pair of electrons can be an additional strategy to induce intrinsic and switchable polarization in rare-earth orthoferrites containing magnetic rare-earth ions.

4 Conclusions

$PrFeO_3$ ceramic samples, substituted progressively (up to 50 mol%) with larger-sized Bi^{3+} (equipped with a stereochemically active lone pair) in place of Pr, have been successfully synthesized by fine-tuning the synthesis conditions. The Fe–O bond lengths elongated with increased Bi content, and the FeO_6 octahedra tilt around the pseudocubic [111] direction was retained, possibly due to the repulsions generated by the stereochemically active lone pair on bismuth. Bi's inclusion created local site disorder and promoted the reduction of more Fe^{3+} to Fe^{2+}, creating higher oxygen vacancies. The randomized distribution of Fe^{3+}, Fe^{2+}, and oxygen vacancies resulting from incremental Bi^{3+}-substitution caused a minor disruption in the antiferromagnetic superexchange interactions, thereby reducing the overall magnetization. At room temperature, a negative exchange bias effect was observed in the $Pr_{0.70}Bi_{0.30}FeO_3$ sample. A spin reorientation transition temperature (T_{SR}) at ~101 K was observed for the $Pr_{0.70}Bi_{0.30}FeO_3$ sample at lower magnetic fields (below 0.02 T). The room-temperature dielectric constant increased with increasing bismuth content in $PrFeO_3$. The DFT calculations predicted an electric field-induced polarization resulting from the asymmetric charge distribution around Bi^{3+}. The intrinsic and switchable polarization (0.17 μC cm^{-2}) was experimentally verified for the Bi-substituted sample after PUND measurements. The multifunctionality invoked upon Bi^{3+}-incorporated $PrFeO_3$ can be mimicked in other perovskites, forming an effective strategy for exploring untapped functions. The properties exhibited by Bi-substituted $PrFeO_3$ can find practical applicability in magnetically modulated transducers, spintronics, ceramic capacitors, chemical sensors, and optoelectronic devices.

Author contributions

Shivangi Rao – methodology, data curation, writing the original draft; Subhajit Sau – methodology, validation, investigation; V. Kanchana – supervision, resources, formal analysis; G. Vaitheeswaran – supervision, resources, formal analysis; Rajamani Nagarajan – supervision, conceptualization, funding acquisition, writing – review and editing.

Data availability

The data supporting this study are included within the article and/or the ESI.†

Conflicts of interest

There are no conflicts to declare.

Acknowledgements

The authors acknowledge the financial support by the SERB (Govt. of India) with file no. CRG/2021/000248 and the Institution of Eminence Grant (IoE/2024-25/12/FRP) from University of Delhi to carry out this research work. Shivangi Rao and Subhajit Sau thank the Council Scientific Industrial Research (CSIR) and MHRD Govt. of India for the research fellowship. G. V. would like to thank CMSD and UOH for providing the computational facility and the institute of Eminence, University of Hyderabad (UOH-IOE-RC3-21-675 046), for their financial support. The authors

sincerely thank Prof. Arumugum Thamizhavel and Mr Ganesh Jangam of TIFR, Mumbai for their help with the magnetic measurements. We acknowledge National Supercomputing Mission (NSM) for providing computing resources of 'PARAM Porul' at NIT Tiruchirappalli, which is implemented by C-DAC and supported by the Ministry of Electronics and Information Technology (MeitY) and Department of Science and Technology (DST), Government of India.

Notes and references

1 Y. Shimakawa, *Perovskite structure compounds*, John Wiley & Sons, 2017.
2 R. J. Tilley, *Perovskites: Structure-property relationships*, John Wiley & Sons, 2016.
3 C. N. R. Rao and B. Raveau, *Transition metal oxides: Structure, properties, and synthesis of ceramic oxides*, Wiley-VCH, Weinheim, 1998.
4 C. N. R. Rao and J. Gopalakrishnan, *New directions in solid state chemistry*, Cambridge University Press, 1997.
5 A. K. Jena, A. Kulkarni and T. Miyasaka, *Chem. Rev.*, 2019, **119**, 3036–3103.
6 K. Y. Tsui, N. Onishi and R. F. Berger, *J. Phys. Chem. C*, 2016, **120**, 23293–23298.
7 D. Kan, C. J. Long, C. Steinmetz, S. E. Lofland and I. Takeuchi, *J. Mater. Res.*, 2012, **27**, 2691–2704.
8 C.-H. Yang, D. Kan, I. Takeuchi, V. Nagarajan and J. Seidel, *Phys. Chem. Chem. Phys.*, 2012, **14**, 15953–15962.
9 D. Kan, L. Pálová, V. Anbusathaiah, C. J. Cheng, S. Fujino, V. Nagarajan, K. M. Rabe and I. Takeuchi, *Adv. Funct. Mater.*, 2010, **20**, 1108–1115.
10 A. Moskvin, *Magnetochemistry*, 2021, **7**, 111.
11 R. Saha, A. Sundaresan and C. N. R. Rao, *Mater. Horiz.*, 2014, **1**, 20–31.
12 S. Ning, A. Kumar, K. Klyukin, E. Cho, J. H. Kim, T. Su, H.-S. Kim, J. M. LeBeau, B. Yildiz and C. A. Ross, *Nat. Commun.*, 2021, **12**, 4298.
13 M. Shang, C. Zhang, T. Zhang, L. Yuan, L. Ge, H. Yuan and S. Feng, *Appl. Phys. Lett.*, 2013, **102**, 062903.
14 Y. Tokunaga, N. Furukawa, H. Sakai, Y. Taguchi, T.-H. Arima and Y. Tokura, *Nat. Mater.*, 2009, **8**, 558–562.
15 J.-H. Lee, Y. K. Jeong, J. H. Park, M.-A. Oak, H. M. Jang, J. Y. Son and J. F. Scott, *Phys. Rev. Lett.*, 2011, **107**, 117201.
16 C. Zhang, M. Shang, M. Liu, T. Zhang, L. Ge, H. Yuan and S. Feng, *J. Alloys Compd.*, 2016, **665**, 152–157.
17 Y. Tokunaga, S. Iguchi, T.-h. Arima and Y. Tokura, *Phys. Rev. Lett.*, 2008, **101**, 097205.
18 B. Rajeswaran, D. Sanyal, M. Chakrabarti, Y. Sundarayya, A. Sundaresan and C. N. R. Rao, *Europhys. Lett.*, 2013, **101**, 17001.
19 K. Dey, A. Indra, S. Mukherjee, S. Majumdar, J. Strempfer, O. Fabelo, E. Mossou, T. Chatterji and S. Giri, *Phys. Rev. B*, 2019, **100**, 214432.
20 N. Aparnadevi, K. Saravana Kumar, M. Manikandan, D. Paul Joseph and C. Venkateswaran, *J. Appl. Phys.*, 2016, **120**, 034101.
21 H. J. Zhao, W. Ren, Y. Yang, X. M. Chen and L. Bellaiche, *J. Phys.: Condens. Matter*, 2013, **25**, 466002.
22 H. J. Zhao, Y. Yang, W. Ren, A.-J. Mao, X. M. Chen and L. Bellaiche, *J. Phys.: Condens. Matter*, 2014, **26**, 472201.
23 E. Martínez-Aguilar, H. Hmŏk, J. Ribas-Ariño, J. M. Siqueiros Beltrones and R. Lozada-Morales, *Int. J. Quantum Chem.*, 2021, **121**, e26551.
24 O. Rosales-González, F. Sánchez-De Jesús, F. Pedro-García, C. A. Cortés-Escobedo, M. Ramírez-Cardona and A. M. Bolarín-Miró, *Materials*, 2019, **12**, 2054.
25 Q. Yao, C. Tian, Z. Lu, J. Wang, H. Zhou and G. Rao, *Ceram. Int.*, 2020, **46**, 20472–20476.
26 N. Imam, G. Aquilanti, A. Azab and S. E. Ali, *J. Mater. Sci.: Mater. Electron.*, 2021, **32**, 3361–3376.
27 T. Pikula, J. Dzik, P. Guzdek, M. Kowalczyk, K. Siedliska and E. Jartych, *Ceram. Int.*, 2020, **46**, 1804–1809.
28 Y. Ma, H. Shen, Y. Fang, H. Geng, Y. Zhao, Y. Li, J. Xu and Y. Ma, *Magnetochemistry*, 2023, **9**, 45.
29 K. Bharati, P. R. Tiwari, R. P. Singh, A. Singh, B. C. Yadav, M. P. Singh and S. Kumar, *Appl. Nanosci.*, 2024, **14**, 277–289.
30 B. H. Toby, *J. Appl. Crystallogr.*, 2001, **34**, 210–213.
31 P. Hohenberg and W. Kohn, *Phys. Rev.*, 1964, **136**, B864.
32 W. Kohn and L. J. Sham, *Phys. Rev.*, 1965, **140**, A1133.
33 P. E. Blöchl, *Phys. Rev. B*, 1994, **50**, 17953.
34 G. Kresse and J. Furthmüller, *Phys. Rev. B*, 1996, **54**, 11169.
35 G. Kresse and D. Joubert, *Phys. Rev. B*, 1999, **59**, 1758.
36 J. P. Perdew, A. Ruzsinszky, G. I. Csonka, O. A. Vydrov, G. E. Scuseria, L. A. Constantin, X. Zhou and K. Burke, *Phys. Rev. Lett.*, 2008, **100**, 136406.
37 S. L. Dudarev, G. A. Botton, S. Y. Savrasov, C. J. Humphreys and A. P. Sutton, *Phys. Rev. B*, 1998, **57**, 1505.
38 D. Stoeffler and Z. Chaker, *J. Magn. Magn. Mater.*, 2017, **442**, 255–264.
39 I. Ameri, A. Boularaf, F. Drief, A. Zaoui and S. Kacimi, *J. Magn. Magn. Mater.*, 2021, **537**, 168214.
40 M. Pugaczowa-Michalska and J. Kaczkowski, *J. Mater. Sci.*, 2015, **50**, 6227–6235.
41 H. J. Monkhorst and J. D. Pack, *Phys. Rev. B*, 1976, **13**, 5188.
42 A. M. Ganose, A. J. Jackson and D. O. Scanlon, *J. Open Source Software*, 2018, **3**, 717.
43 R. D. King-Smith and D. Vanderbilt, *Phys. Rev. B*, 1993, **47**, 1651.
44 D. Vanderbilt and R. D. King-Smith, *Phys. Rev. B*, 1993, **48**, 4442.
45 Z. Zhou, L. Guo, H. Yang, Q. Liu and F. Ye, *J. Alloys Compd.*, 2014, **583**, 21–31.
46 F. A. Mir, M. Ikram and R. Kumar, *Vib. Spectrosc.*, 2011, **55**, 307–310.
47 E. Traversa, P. Nunziante, L. Sangaletti, B. Allieri, L. E. Depero, H. Aono and Y. Sadaoka, *J. Am. Ceram. Soc.*, 2000, **83**, 1087–1092.
48 F. Chang, S. Yuan, X. Wang, Y. Cao, B. Lu and S. Cao, *Solid State Commun.*, 2012, **152**, 168–172.
49 E. Chatla, N. Vankudothu, S. Shravan Kumar Reddy, S. Shanmukharao Smatham, M. Sreenath Reddy, C. Gopal Reddy and P. Yadagiri Reddy, *Appl. Phys. A*, 2024, **130**, 10.

50 C.-S. Tu, C.-S. Chen, P.-Y. Chen, Y. L. Hsieh, R. R. Chien, V. H. Schmidt, K.-C. Feng and H.-W. Chang, *J. Alloys Compd.*, 2018, **768**, 903–913.
51 S. Ward, M. A. Isaacs, G. Gupta, M. Mamlouk and S. S. Pramana, *Sustainable Energy Fuels*, 2021, **5**, 154–165.
52 S. Lütkehoff, M. Neumann and A. Ślebarski, *Phys. Rev. B*, 1995, **52**, 13808.
53 G. H. Major, N. Fairley, P. Sherwood, M. R. Linford, J. Terry, V. Fernandez and K. Artyushkova, *J. Vac. Sci. Technol., A*, 2020, **38**, 061203.
54 T. J. Frankcombe and Y. Liu, *Chem. Mater.*, 2023, **35**, 5468–5474.
55 J. Wang, D. N. Mueller and E. J. Crumlin, *J. Eur. Ceram. Soc.*, 2024, **44**, 116709.
56 B. Jiang, L. Li, Q. Zhang, J. Ma, H. Zhang, K. Yu, Z. Bian, X. Zhang, X. Ma and D. Tang, *J. Mater. Chem. A*, 2021, **9**, 13008–13018.
57 X. Zhang, C. Pei, X. Chang, S. Chen, R. Liu, Z.-J. Zhao, R. Mu and J. Gong, *J. Am. Chem. Soc.*, 2020, **142**, 11540–11549.
58 M. Pires, C. Israel, W. Iwamoto, R. Urbano, O. Agüero, I. Torriani, C. Rettori, P. Pagliuso, L. Walmsley and Z. Le, *et al.*, *Phys. Rev. B*, 2006, **73**, 224404.
59 A. Egorysheva, O. Ellert, O. Gajtko, A. Berseneva, Y. V. Maksimov and R. Svetogorov, *Ceram. Int.*, 2016, **42**, 13976–13982.
60 L. Boudad, M. Taibi, W. Belayachi and M. Abd-Lefdil, *J. Solid State Chem.*, 2022, **309**, 122933.
61 X.-H. Zhu, X.-B. Xiao, X.-R. Chen and B.-G. Liu, *RSC Adv.*, 2017, **7**, 4054–4061.
62 Q. Yang, H. Qin, K. Huang, R. Zhang, L. Yang, Z. Lu, Q. Yao, L. Cheng, C. Huang and Q. Long, *et al.*, *J. Magn. Magn. Mater.*, 2023, **565**, 170274.
63 J.-S. Zhou, L. Marshall, Z.-Y. Li, X. Li and J.-M. He, *Phys. Rev. B*, 2020, **102**, 104420.
64 D. Triyono, S. Fitria and U. Hanifah, *RSC Adv.*, 2020, **10**, 18323–18338.
65 V. L. Mathe, *J. Magn. Magn. Mater.*, 2003, **263**, 344–352.
66 B. V. Prasad, G. N. Rao, J. Chen and D. S. Babu, *Solid State Sci.*, 2012, **14**, 225–228.
67 S. Katba, S. Jethva, G. Panchal, R. Choudhary, D. Phase and D. Kuberkar, *J. Alloys Compd.*, 2019, **789**, 814–824.
68 J. Sheikh, S. A. Acharya and U. P. Deshpande, *Mater. Chem. Phys.*, 2020, **242**, 122457.
69 D. Sanghvi, H. Boricha, B. Hirpara, S. Solanki, V. Shrimali, A. Joshi, P. Solanki and N. Shah, *J. Sol-Gel Sci. Technol.*, 2020, **93**, 666–677.
70 R. Shukla, R. Dhaka, S. Dash, S. C. Sahoo, B. Bahera, P. Babu, R. Choudhary and A. K. Patra, *et al.*, *Ceram. Int.*, 2020, **46**, 8730–8744.
71 I. Makoed, N. Liedienov, A. Pashchenko, G. Levchenko, D. Tatarchuk, Y. Didenko, A. Amirov, G. Rimski and K. Yanushkevich, *J. Alloys Compd.*, 2020, **842**, 155859.
72 Y. Zhang, J. Sun, J. P. Perdew and X. Wu, *Phys. Rev. B*, 2017, **96**, 035143.
73 A. Panchwanee, V. R. Reddy and A. Gupta, *J. Magn. Magn. Mater.*, 2018, **448**, 38–42.
74 J. Ramesh, N. Raju, S. S. K. Reddy, M. S. Reddy, C. G. Reddy, P. Y. Reddy, K. R. Reddy and V. R. Reddy, *J. Alloys Compd.*, 2017, **711**, 300–304.